Classification of Dynamic Vulnerable Road Users Using a Polarimetric mm-Wave MIMO Radar

Bouwmeester, Wietse; Fioranelli, Francesco; Yarovoy, Alexander

DOI
10.1109/TRS.2025.3527884

Publication date
2025

Document Version
Final published version

Published in
IEEE Transactions on Radar Systems

Classification of Dynamic Vulnerable Road Users Using a Polarimetric mm-Wave MIMO Radar

Wietse Bouwmeester, *Member, IEEE*, Francesco Fioranelli, *Senior Member, IEEE*, and Alexander G. Yarovoy, *Fellow, IEEE*

***Abstract*— In this article, the classification of dynamic vulnerable road users (VRUs) using polarimetric automotive radar is considered. To this end, a signal processing pipeline for polarimetric automotive MIMO radar is proposed, including a method to enhance angular resolution by combining data from all polarimetric channels. The proposed signal processing pipeline is applied to measurement data of three different types of VRUs and a car, collected with a custom automotive polarimetric radar, developed in collaboration with Huber+Suhner AG. Several polarimetric features are estimated from the range–velocity signatures of the measured targets and are subsequently analyzed. A Bayesian classifier and a convolutional neural network (CNN) using these estimated polarimetric features are proposed and their performance is compared against their single-polarized counterparts. It is found that for the Bayesian classifier, a significant increase in classification performance is achieved, compared to the same classifier using single polarized information. For the CNN-based classifier, utilizing the distribution of polarimetric features of the target's range–velocity signatures also increases classification performance, compared to its single-polarized version. This shows that polarimetric information is valuable for classification of VRUs and objects of interest in automotive radar.**

***Index Terms*— Automotive radar, classification, polarimetry, vulnerable road users (VRUs).**

I. Introduction

In RECENT years, increasingly more vehicles are equipped with 77 GHz automotive radar to enable advanced driving assistance systems such as adaptive cruise control, but also to enhance road safety. The increased integration of these radar systems in vehicles has the potential to also benefit other road users besides the driver of the vehicle itself. Specifically, this is true for vulnerable road users (VRUs), which typically include pedestrians and cyclists. They are particularly vulnerable when involved in accidents as they do not have any protective structures or devices that help dissipating the force of impact, which cars, in contrast, are equipped with. Because of their vulnerability in combination with, among others, the ever-increasing safety requirements on cars, in the Netherlands most fatal traffic victims are currently cyclists, having overtaken car occupants in recent years [1].

Received 8 August 2024; revised 5 November 2024 and 2 January 2025; accepted 6 January 2025. Date of publication 9 January 2025; date of current version 20 January 2025. *(Corresponding author: Wietse Bouwmeester.)*

The authors are with the Microwave Sensing Signals and Systems (MS3) Group, Department of Microelectronics, TU Delft, 2628 CD Delft, The Netherlands (e-mail: w.bouwmeester@tudelft.nl; f.fioranelli@tudelft.nl; a.yarovoy@tudelft.nl).

Digital Object Identifier 10.1109/TRS.2025.3527884

Because of this vulnerability of cyclists, pedestrians, and other VRUs, many research efforts concerned with using automotive radar to detect and classify VRUs have been undertaken in recent years. For example, in [2], [3], and Pérez et al. [4], deep learning methods are employed. In [2] and [3], time–frequency, i.e., micro-Doppler signatures, are used for this, while [4] uses a single range-Doppler frame. Using a convolutional network, a classification accuracy of 84.2% was achieved on unseen data in [4], while the convolutional neural network (CNN) presented in [3] achieved classification accuracy values greater than 92.4%. In [5], classification of VRUs is performed using autocorrelation features in the time–frequency domain. It is found that the features of correlation length and time show high potential for classification of pedestrians and cyclists. In [6], pedestrian classification is performed using image features which are extracted from range-Doppler maps. Combining this with tracking algorithms resulted in a success rate of 88%, using a sensing signal bandwidth of 1.6 GHz.

Similar to the automotive radar systems that are currently available, the radar used in the aforementioned research employed single-polarized sensing waves. These systems are unable to measure the polarization state of the waves backscattered from the environment and targets, which may contain useful information for classification purposes. For example, the spokes of a bicycle wheel could be sensitive to one type of polarization, while relatively insensitive to another due to their inherent vertical structure. Thus, to exploit the information available in the polarization state, polarimetric radar systems are required. However, currently, there are no commercially available automotive radar systems on the market, and only recently fully polarimetric automotive radar prototypes and proof-of-concepts have been developed for research purposes [7], [8], [9], [10], [11], [12]. In [7] and [8], two antenna concepts for polarimetric automotive radar are presented, while Trummer et al. [9], Zang et al. [10], and Tinti et al. [11] propose three fully integrated radar systems. In [12], an instrumentation radar is presented to study scattering behavior from VRUs at frequencies within the automotive radar band.

Even though the use of polarimetry in automotive radar is quite novel and literature on the topic is relatively limited, a few studies have already been undertaken to study the polarimetric response of VRUs at 77 GHz. In [13] and [14], several polarimetric representations of targets have been investigated for the purpose of VRU classification using a modified version of the approach presented in [15]. Using different polarimetric

features in point cloud format, it is found that a significant improvement in VRU classification can be achieved over exclusively using nonpolarimetric features. This is extended further in [16], where detection of road users is performed on predetector data, showing further improvements in classification performance. In both works, classification is performed predominantly in the angular domain and only the strongest Doppler measurements corresponding to targets are kept. The radar system used in these works was also employed to investigate the benefits of polarimetric information for localization purposes [17]. In [18], static polarimetric measurements of four different types of bicycles were carried out at various azimuth angles. Here, it is also concluded from the results that polarimetric information could potentially help improve vehicle classification. In [19], static measurements of a number of vehicles as well as a motorcycle, bicycle, and pedestrian were performed and it is found that significant differences in polarimetric returns can occur depending on target orientation. In [20], a classifier based on a CNN is used to classify static canonical targets (dihedrals and boxes) in various orientations, and classification accuracy over 90% is obtained. In [12], partially polarimetric measurements of moving VRUs such as pedestrians, a bicycle, and a dog are presented. It was found that the range-Doppler signatures presented a number of unique velocity-dependent features that potentially could be used for classification.

However, to the best of the authors' knowledge, in none of the aforementioned research the impact of the dynamic behavior of VRUs (e.g., moving arms/legs with related Doppler signature) on their polarimetric response and its use for classification purposes is extensively considered. In this article, this gap is addressed by further studying the polarization of the returns from cyclists, pedestrians, motorcyclists, and a vehicle while they are moving. To achieve this, a custom-designed novel polarimetric MIMO automotive radar system was developed in collaboration with Huber+Suhner AG (H+S) to collect measurement data from these classes of targets while they were moving in various direction with respect to the radar. The collected measurement data is subsequently processed and analyzed using a new polarimetric automotive radar signal processing pipeline. From these data, it is found that polarimetric signatures of VRUs differ significantly from each other and that the polarimetric composition of their returns changes over time. Moreover, the polarimetric ratios of the considered classes of targets form clusters, indicating that the polarization state of their returns may contain useful information for classification. It is also shown that the range–velocity signatures of pedestrians and cyclists contain some polarimetric structure, which could potentially be exploited by machine learning algorithms to improve classification.

The rest of this article is organized as follows. Section II introduces the signal processing required for time division multiplexing (TDM) MIMO polarimetric radar systems. Section III introduces the polarimetric radar system including a new calibration method based on a radar target simulator, as well as the data collection. Section IV describes the postprocessing procedures applied to the experimental measurement data, with results in Section V. Conclusions are drawn in Section VI.

II. Polarimetric MIMO Radar Signal Processing

In this section, the processing of the received waveforms of a polarimetric MIMO frequency modulated continuous wave (FMCW) radar with TDM is considered. First, the processing of the individual polarimetric channels is discussed, and subsequently coherent processing of all virtual channels is considered to enhance the angular resolution.

A. Single Polarimetric Channel Processing

In contrast to single-polarized radar, polarimetric radar systems also aim to estimate the scattering parameters of a target. The scattering matrix describes the relation between the polarization and amplitude of the electric fields, indicated by E, of an incident sensing wave impinging on a target and the wave scattered back by that target, as shown in the following equation:

$$\begin{bmatrix} E_x^s \\ E_y^s \end{bmatrix} = \begin{bmatrix} S_{xx} & S_{xy} \\ S_{yx} & S_{yy} \end{bmatrix} \begin{bmatrix} E_x^{\text{inc}} \\ E_y^{\text{inc}} \end{bmatrix}. \tag{1}$$

Here, the superscript s indicates the scattered components of the wave while the superscript inc indicates the incident wave. The subscripts x and y indicate the polarization basis, for example, a horizontal/vertical or left/right-hand circular basis. In the case of a horizontal/vertical basis, x could be for instance substituted by H, representing the horizontal component, while y is substituted by V, representing the vertical component, whereas for a left/right-hand circular basis x and y could be substituted by L and R representing the left-hand and right-hand circularly polarized components, respectively.

Subsequently, the relationship between the incident sensing wave and the scattered wave can be used to formulate the signal model of the data collected by a polarimetric FMCW radar system. The waveform transmitted corresponding to the ith virtual channel as a function of time t by an FMCW radar is shown in the following equation:

$$\begin{aligned} s_i^{tx}(t) &= e^{j2\pi \int \left(f_{\text{start}} + f_{\text{slope}} t\right)\, dt} \\ &= e^{2\pi j \left(f_{\text{start}} + \frac{1}{2} f_{\text{slope}} t\right) t} \end{aligned} \tag{2}$$

where f_{start} is the frequency at which the chirp signal starts and f_{slope} the frequency slope of the chirp ramp.

This transmitted waveform reaches the target after some propagation delay and incurring free space losses, and is then scattered back toward the radar, eventually reaching the receiving antennas with an additional propagation delay and more free space losses. Thus the received waveform s_i^{rx} at the ith virtual xy-polarized channel, i.e., a virtual channel with an x-polarized receiving channel and a y-polarized transmitting antenna, can be modeled as shown in the following equation:

$$s_i^{rx}(t, \Delta t_i) = \text{LS}_{xy} e^{2\pi j \left(f_{\text{start}} + \frac{1}{2} f_{\text{slope}} (t - \Delta t_i)\right)(t - \Delta t_i)}. \tag{3}$$

Here, L denotes the total propagation losses and Δt_i indicates the total propagation delay to and back from a target. Note that in order to find the received waveform for other polarimetric channels, the x and y subscripts can be replaced by

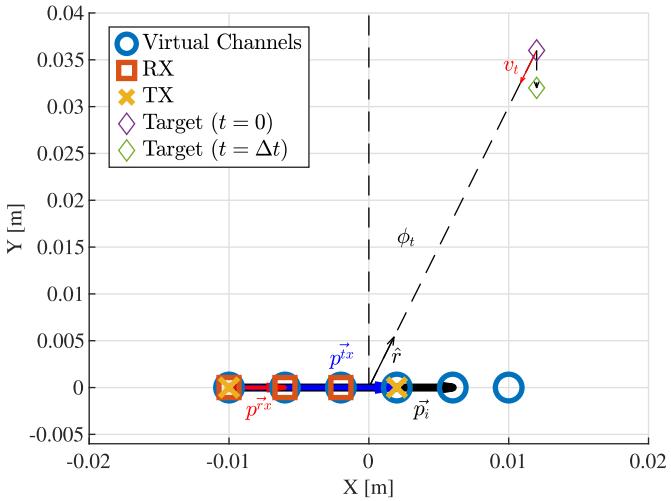

Fig. 1. Schematic of the problem geometry. Note that the virtual array has been translated so that it is centered on the x-axis after the summation of the sets of $\vec{p^{tx}}$ and $\vec{p^{rx}}$ for each virtual element. Also, as this schematic shows the top view of the problem, the elevation angle θ_t is not visible.

subscripts of the corresponding polarimetric channels, e.g., S_{xx} for the xx-polarized channel. In order to keep the equations as tractable as possible, only the equations for the xy-polarized channel are shown within this article.

To compute the total propagation delay for a measured channel, the problem geometry shown in Fig. 1 is considered. Note that in this schematic drawing, the virtual array resulting from the summation of the sets of $\vec{p^{tx}}$ and $\vec{p^{rx}}$ corresponding to each virtual element is translated, so that it is centered on the x-axis. As long as far-field conditions are satisfied, this does not impact the resulting total propagation delay, since the target angles as seen from each virtual element are approximately equal to each other. Also, since the target's velocity should be within the maximum unambiguous velocity range and since the target should be located in the far-field region, the target angles of the target at $t = 0$ and $t = \Delta t$ are approximately equal too. It can be seen from Fig. 1 that the total propagation delay is a function of the start range r_0 of a target from the origin of the virtual array formed by the radar system, its radial velocity with respect to the radar v_t, elevation θ_t, and azimuth ϕ_t, as shown in the following equation:

$$\Delta t_i(r_0, v_t, \theta_t, \phi_t) = 2\frac{r_0 + v_t T_i(n)}{c} + \frac{\hat{r}(\theta_t, \phi_t) \cdot \vec{p_i}}{c}. \tag{4}$$

As can be seen in (4), Δt_i is also dependent on the location of the ith virtual channel $\vec{p_i}$ in the virtual array which is the sum of $\vec{p^{tx}}$ and $\vec{p^{rx}}$, which respectively are the positions of the transmitting antenna $\vec{p^{tx}}$ and the receiving antenna $\vec{p^{rx}}$ corresponding to that virtual channel. Furthermore, c indicates the propagation velocity of electromagnetic waves and $T_i(n)$ represents the time elapsed since the first chirp of the sequence, in order to account for the range migration of a target due to its radial velocity with respect to the radar. Note that T_i itself depends on the chirp number n, the interchirp duration T_{chirp} as well as a time offset ΔT_i as shown in the following equation:

$$T_i(n) = nT_{\text{chirp}} + \Delta T_i. \tag{5}$$

This time offset results from the TDM operation of the radar. Namely, when the transmitters of the radar operate in an interleaved fashion, the chirps corresponding to the virtual channels using the second transmitter lag behind one interchirp duration. This results in turn the virtual channels corresponding to the third transmitter to have an offset of two interchirp durations, and so forth for all the other available transmitters.

Furthermore, $\hat{r}$ is the unit vector that indicates the angle of arrival of the wave and is dependent on the elevation and azimuth of a target as shown in the following equation:

$$\hat{r}(\theta_t, \phi_t) = \begin{bmatrix} \cos\theta_t \sin\phi_t \\ \cos\theta_t \cos\phi_t \\ \sin\theta_t \end{bmatrix}. \tag{6}$$

In an FMCW radar system, the received signal is subsequently de-chirped by means of complex mixing it with the transmitted signal. This results in the final signal model of the ith virtual channel s_i as sampled by the ADCs corresponding to that channel. This can be mathematically written as shown in the following equation:

$$\begin{aligned} s_i(t, \Delta t_i) &= s_i^{rx}(t, \Delta t_i)^* s_i^{tx}(t) \\ &= \text{LS}_{xy} e^{2\pi j\left(f_{\text{start}}\Delta t_i - \frac{1}{2} f_{\text{slope}}\Delta t_i^2\right)} e^{2\pi j f_{\text{slope}} t \Delta t_i}. \end{aligned} \tag{7}$$

In (7), superscript * indicates the complex conjugate operator.

Using this signal model, the signal processing pipeline to estimate the range, radial velocity, elevation, azimuth, and scattering parameters of a target for a single polarimetric channel can be developed. First, the signal model can be simplified by using the assumption that $f_{\text{start}}\Delta t_i \gg (1/2) f_{\text{slope}}\Delta t_i^2$. This assumption is typically valid for mm-wave automotive radar, as the sampled bandwidth of the chirp is much smaller than the start frequency; for example, the maximum available bandwidth in this band is 4 GHz, while the minimum start frequency is 76 GHz. Furthermore, the full 4 GHz bandwidth is not usually sampled in its entirety, as this would require high-performance ADCs, whereas lower performing but cheaper ADCs can generally provide the required sample rates necessary to achieve, among others, adequate unambiguous range. Applying the aforementioned assumption results in the following equation:

$$s_i(t, \Delta t_i) = \text{LS}_{xy} e^{2\pi j f_{\text{start}}\Delta t_i} e^{2\pi j f_{\text{slope}} t \Delta t_i}. \tag{8}$$

Combining (4) and (8) and performing a Fourier transform over t, r_0 of the target can be recovered given that $2(r_0/c) \gg 2(v_t T_i/c) + (\hat{r}\vec{p}_i/c)$, which is valid as r_0 is the dominant term of the propagation delay. This results in the following equation:

$$s_i^r = \text{LS}_{xy} e^{2\pi j f_{\text{start}}\left(2\frac{r_0 + v_t T_i}{c}\right) + j\vec{k}\vec{p}_i} \delta(r - r_0). \tag{9}$$

Here, $\vec{k}$ represents the wave vector and is defined as $(2\pi/\lambda)\hat{r}$, where λ is the wavelength at the start frequency of the chirp.

Subsequently, the target's radial velocity can be determined by performing a Fourier transform over n, which corresponds to a transform over the sequence of chirps belonging to

the considered virtual channel. This results in the following equation:

$$s_i = \mathrm{LS}_{xy} e^{2\pi j f_{\text{start}} \left(2\frac{r_0 + v_t \Delta T_i}{c}\right) + j\vec{k}\vec{p}_i} \delta(v - v_t)\delta(r - r_0). \quad (10)$$

Note that the channel time offset term in (10) introduces an additional velocity-dependent phase shift between channels. This phase shift appears due to range migration of a moving target in between the starts of multiple different chirp sequences belonging to virtual channels because of the TDM used by the radar system to preserve waveform orthogonality. If left uncompensated, this additional phase shift leads to an additional error in the estimation of the phase of the scattering parameter measured by the corresponding virtual channel.

As the aforementioned phase shift is solely dependent on the target's radial velocity and the channel time offset, which are known quantities after the estimation step in (10), it can be compensated by multiplying each range/velocity bin by a factor of $e^{-4\pi j f_{\text{start}}(v/c)\Delta T_i}$, similar to the approach presented in [21]. This leads to the following equation:

$$s_i = \mathrm{LS}_{xy} e^{4\pi j f_{\text{start}} \frac{r_0}{c} + j\vec{k}\vec{p}_i} \delta(v - v_t)\delta(r - r_0). \quad (11)$$

Subsequently, the azimuth and elevation of the target can be estimated. This can be done by means of Fourier transformation over virtual channels belonging to the same polarimetric channel when they are uniformly spaced, so that the backscattered wavefront of a target is uniformly sampled in space. This is similar to estimation of target range and velocity where the aforementioned wavefront is sampled uniformly in time rather than in space. When the virtual channels are not spaced uniformly, the target azimuth and elevation can be estimated using digital beam forming instead. This procedure is mathematically shown in the following equation:

$$s = \frac{\mathrm{LS}_{xy}\delta(v - v_t)\delta(r - r_0)}{N} \sum_{i=1}^{N} e^{4\pi j f_{\text{start}} \frac{r_0}{c} + j\vec{k}\vec{p}_i} e^{j\vec{\beta}_i}. \quad (12)$$

In this equation, N is the total number of virtual channels belonging to a specific polarimetric channel and $\vec{\beta}_i$ represents the steering vector which is defined as shown in the following equation:

$$\vec{\beta}(\theta, \phi) = -\frac{2\pi}{\lambda} \begin{bmatrix} \cos\theta \sin\phi \\ \cos\theta \cos\phi \\ \sin\theta \end{bmatrix} \vec{p}_i. \quad (13)$$

When the steering vector aligns with the wave vector, the magnitude of the summation in (12) will be maximum, and thus the azimuth and elevation of a target are found.

Now that the target's range, velocity, elevation, and azimuth have been estimated, the amplitude and phase of s are the product of the propagation losses L, the scattering parameters S_{xy}, and a residual phase term $e^{4\pi j f_{\text{start}}(r_0/c)}$. As for determining the scattering matrix, only the relative phase of the scattering parameters is of importance, the residual phase term can be eliminated by subtracting the phase of the first scattering parameter from all four elements of the scattering matrix, since r_0 is independent of the polarimetric channel. Furthermore, the propagation losses are dominated by r_0 and thus are also independent of polarization. Therefore, this term can be compensated for by using the radar equation [22].

Thus, after the compensation of the residual phase term and the propagation losses, the amplitude and phase values for each range–angle–velocity bin remain, and they represent the scattering parameter corresponding to the polarimetric channel. The final scattering matrix for each range–angle–velocity bin is then subsequently found by combining the scattering parameters of all polarimetric channels.

Using the processing procedure presented in this section, the range, velocity, and angular resolutions for each polarimetric channel are equal to those found for a single-polarized radar system with the same array topology as the corresponding polarimetric subarray. Therefore, the angular resolution that can be achieved by a single polarimetric subarray within a polarimetric radar system with a certain amount of total virtual channels is generally lower compared to a single-polarized radar system with the same amount of total virtual channels. This is because in order to implement polarimetric diversity, some of these virtual channels need to be dedicated to the orthogonal polarization.

B. Combined Polarimetric Channel Processing

As the total aperture of a polarimetric MIMO radar system is subdivided into multiple polarimetric channels, the angular resolution of each polarimetric channel is limited by the aperture corresponding to that specific polarimetric channel. The coupling between the scattering parameters and angle that is present when processing all channels together, as if it were a single polarimetric radar system, leads to errors in the estimation of target azimuth and elevation. This usually results in coarser angular resolution for a polarimetric radar when compared to a single-polarized radar system with the same amount of total virtual channels.

However, the signals received by the individual polarimetric channels can be combined to increase the resulting angular resolution compared to the resolution in a single polarimetric channel. A method to accomplish this, based on the assumption that only one dominant target is present per range–velocity bin, is shown schematically in Fig. 2.

As shown in Fig. 2, first the single polarimetric channel processing described in Section II-A is performed to find the scattering parameters corresponding to the four polarimetric channels. Subsequently, a new maximum radar cube s_{combined} is constructed from the maximum of the amplitudes of the radar cubes corresponding to all four polarimetric channels, denoted from s_{xx} to s_{yy}, as shown in the following equation:

$$s_{\text{combined}} = \max(|s_{xx}|, |s_{xy}|, |s_{yx}|, |s_{yy}|). \quad (14)$$

This combined radar cube is then subsequently used to find the azimuth and elevation at which the return with the highest intensity is obtained for each range–velocity bin by taking the maximum over the elevation and azimuth. By combining all polarimetric channels, the correct angles corresponding to a target can still be found if no return is present in one of the channels. Subsequently, for each polarimetric channel, the phase of the scattering parameters is found for each

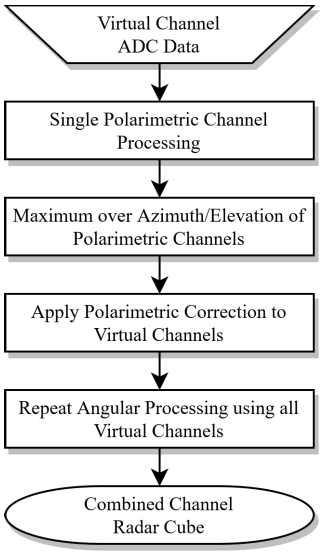

Fig. 2. Block diagram of the proposed combined polarimetric channel processing method to achieve comparable resolution as a single-polarized radar with the same array configuration.

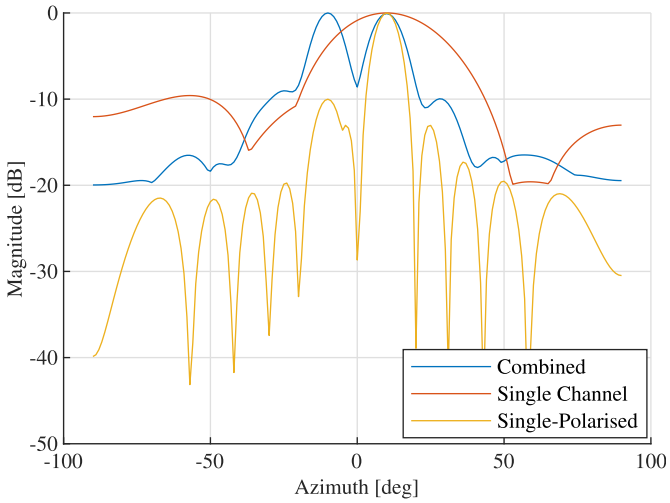

Fig. 3. Simulated azimuth cut of two targets located at $-10°$ and $+10°$, as measured by a single polarimetric channel (red), all polarimetric channels combined using the proposed method (blue), and a single-polarized array of the same dimensions (yellow).

range–velocity bin using the azimuth and elevation of the target found in the last step. The range–velocity spectra of each virtual channel are then corrected for polarimetric effects on the measured phase by subtracting the previously found phase from each corresponding range–velocity bin as shown in the following equation:

$$s_{i,\text{corrected}} = s_i e^{-j\angle S_{xy,\max}}. \tag{15}$$

Here, $s_{i,\text{corrected}}$ indicates the corrected virtual channel radar cube and $S_{xy,\max}$ represents the scattering parameter corresponding to the ith virtual channel, found in the range–velocity bin at the azimuth/elevation angle at which maximum return was found in s_{combined}.

Thereafter, digital beam forming can be applied using all corrected virtual channels to obtain a combined channel radar cube without polarimetric information, but with higher angular resolution compared to single polarimetric channel processing.

The limitation of the proposed combined channel processing method lies in the assumption that only one dominant target is present per range–velocity bin. When this is not satisfied, only the polarimetric phase shift of the strongest target within the range–velocity bin is compensated properly, introducing errors in the estimation of the other targets that are present in that same bin, but at different azimuth and elevation angles. Furthermore, when an observed target does not provide a significant return in all four polarimetric channels and no leakage between the polarimetric channels of the radar system is present, only the channels that show a significant return can be processed together, thus limiting the achievable resolution for this type of targets.

Fig. 3 shows the azimuth cut of a simulated scene with two targets at a range of 15 m. The first and second targets are located at $-10°$ and $+10°$ azimuth, respectively, with velocities of -3 and $+3$ m/s. For simulation purposes, the scattering parameters used for the first and second target were a value of 1 and $\sqrt{10}e^{j(\pi/6)}$ for S_{xx}, respectively, 4 and $10e^{j(\pi/3)}$ for S_{xy}, $\sqrt{10}e^{j(\pi/3)}$ and $4e^{j(\pi/5)}$ for S_{yx}, and $10e^{j(\pi/4)}$ and $e^{j(\pi/2)}$ for S_{yy}. The antenna array used in this simulation is a uniform linear array with 12 virtual channels with half-λ spacing, subdivided equally between the four polarimetric channels. The return as function of azimuth obtained with this array is compared in Fig. 3 with the same array but with all virtual channels belonging to the same polarimetric channel in order to simulate a conventional single-polarized MIMO radar system. This figure also shows the estimated azimuth using a single polarimetric channel. It can be seen that the proposed combined channel processing method provides a similar level of azimuthal resolution compared to single-polarized radar, while also being able to provide coarser-resolution polarimetric information that can be used for classification purposes as demonstrated in Section V. Furthermore, the received power in all polarimetric channels is summed coherently, thus providing better signal-to-noise ratios with respect to a comparable single-polarized antenna measuring a polarimetric channel that only provides weak returns.

III. Experimental Measurements

This section describes the experimental measurements. In Section III-A, the polarimetric radar system is introduced while Section III-B describes the calibration procedure. The data collection procedure is detailed in Section III-C.

A. Polarimetric MIMO Radar System

To perform polarimetric automotive radar measurements, a novel polarimetric MIMO radar system was developed in collaboration with Huber+Suhner (H+S). This radar system is based on Texas Instruments' AWR2243BOOST radar evaluation module, which is equipped with an AWR2243 automotive FMCW radar chip. To enable MIMO radar functionality, the AWR2243 has three transmit channels and four receive channels. Furthermore, the AWR2243BOOST evaluation module is stacked on a Texas Instruments DCA1000 processing board to efficiently transfer the raw data gathered by the AWR2243's ADCs to a computer for further processing. The

TABLE I
WAVEFORM SETTINGS FOR THE RADAR MODULE USED IN THIS WORK

Start Frequency	77 GHz
Frequency Slope	101.388 MHz/μs
ADC Sample Start Time	5.12 μs
ADC Idle Time	7 μs
ADC Sample Rate	22000 ksps
ADC Samples	750
Chirps per Frame	64
Frame Repetition Time	10 ms

radar assembly is subsequently mounted on a tripod, resulting in it being placed at a height of about 65 cm above ground level.

The radar system was programmed to use a high-resolution short-range waveform so that the polarimetric structure of the target-under-test could be investigated. To this end, the AWR2243 chip was set to use a bandwidth of 3.58 GHz, resulting in a range resolution of 4.2 cm. To achieve a maximum unambiguous velocity of 7 m/s in combination with a maximum unambiguous range of 31 m, the AWR2243's maximum sample rate of 22 Ms/s, collecting 750 samples per chirp, in combination with a frequency slope of 101 MHz/μs was utilized. Furthermore, each transmitter was set to transmit 64 chirps in an interleaved fashion to obtain a velocity resolution of 0.22 m/s while keeping the phase change between channels for moving targets caused by TDM (as mentioned in Section II) and target geometry changes as small as possible. A full list of waveform parameters can be found in Table I.

Unlike the regular AWR2243BOOST evaluation module, the polarimetric MIMO radar used for this work features a custom antenna array manufactured using 3-D printing technology by Hubert+Suhner AG [23], [24], [25] instead of series-fed patch arrays with which the standard evaluation module is equipped. The custom antenna array designed by H+S comprises of seven subarrays consisting of eight open-ended waveguide radiators positioned vertically with respect to each other to achieve a narrow beam in the elevation direction. Three of the subarrays function as transmitters, while the other four function as receivers.

To implement polarimetric capabilities, instead of using horizontally oriented open-ended waveguide radiators within a subarray, the radiators are either rotated 45° counterclockwise with respect to the vertical plane of the transmitters, indicated as positive diagonal (PD), or 45° in the opposite direction, indicated as negative diagonal (ND). In this way, an orthogonal polarization basis is created. An advantage provided by this diagonal polarization basis is that the radiation patterns of the ND and PD polarized subarrays are theoretically equal to each other, which can be exploited for calibration purposes. Also, as the ND- and PD-polarized subarrays are mirrored versions of each other, the implementation of both subarrays is simplified. In this article, the measured return obtained by transmitting with a YD-polarized subarray and receiving with an XD-polarized subarray is indicated as an XY-polarized channel. Here, X and Y can be either N for ND or P for PD.

A picture of the fully assembled radar system including the custom-designed 3-D printed antenna can be found in Fig. 4.

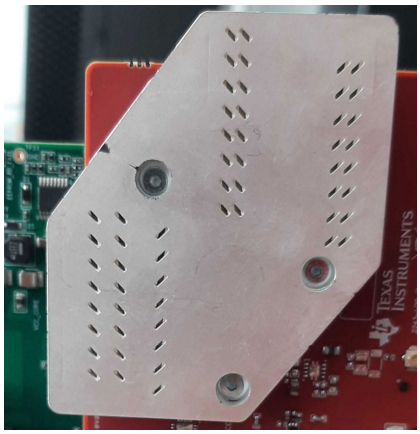

Fig. 4. Picture of the custom polarimetric antenna mounted on a modified AWR2243BOOST evaluation module.

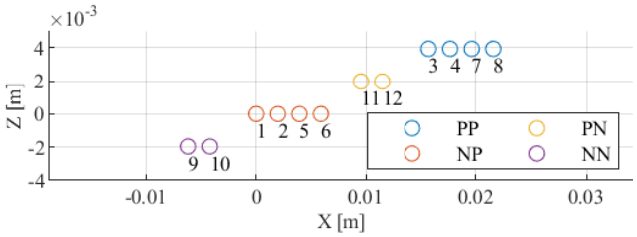

Fig. 5. Virtual array formed by the custom polarimetric antenna as seen in the direction of transmission. The numbers indicate the corresponding virtual channel numbers.

The three subarrays in the lower left corner of the antenna are connected to the transmitting channels of the AWR2243 chip, while the four in the upper right corner correspond to the receiving channels. It can be seen that two of the transmitting channels are PD-polarized, while the remaining one is ND-polarized, and that the four receiving channels are equally split between PD- and ND-polarization. All four differently polarized channels are offset slightly in height to enable estimation of elevation when all polarimetric channels are processed together.

The virtual array formed by the antenna is shown in Fig. 5. It can be seen that the number of virtual channels dedicated to each of the four polarimetric channels is unbalanced due to the uneven number of transmitting channels on the AWR2243 chip. Furthermore, all virtual channels corresponding to a polarimetric channel form dense linear arrays, thus ensuring that each polarimetric channel can be processed individually without creating grating lobes in the visible region. The array achieves a cross-polar isolation in excess of 20 dB at broadside, which decreases when scanning at off-broadside angles [26]. Therefore, the data collection procedures utilized in this work, as presented in Section III-C, are designed to keep the targets as close as practically possible to the radar's broadside direction. Moreover, as the number of virtual channels per polarimetric channel is relatively limited due to the limitations of the AWR2243 chip, the angular resolution of the polarimetric radar is relatively low. Thus, the polarimetric feature analysis and classification study presented in Section V is mainly performed in the range-Doppler domain, as the information in this domain is richer than in the angular domain.

B. Calibration

To eliminate the effects on phase and amplitude variations due to the different feed-line lengths in the antenna subarrays, the radar system must be calibrated. Unfortunately, simple measurements of a corner reflector do not suffice for this purpose, as this target does not change the polarization of the backscattered sensing wave, thus allowing only for calibration of the two co-polarized channels. To solve this issue, multiple different calibration targets with different polarimetric properties need to be used [26], [27].

Alternatively, instead of using passive calibration targets, the radar system can be calibrated with a radar target simulator equipped with a vertically polarized horn antenna. This approach has a few advantages, the first of which is that for a diagonal polarization basis, all polarimetric channels should measure the same scattering parameters, thus removing the need for using multiple different calibration targets. In this way, the potential errors introduced by misalignments between calibration targets are avoided. Furthermore, the definition of an arbitrary phase relation between co- and cross-polarized channels is no longer required. Second, the radar target simulator allows for simulating a target with a given velocity, which increases the measured signal-to-noise ratio of the simulated target, as this is better separated from the static clutter present in the scene.

Because of these advantages, calibration of the radar system was performed in this work using an AREG800A radar target simulator equipped with an AREG8-81S horn antenna front-end manufactured by Rohde&Schwarz. The radar target simulator was configured to simulate two targets at a distance of 24 and 28 m, with velocities of 3 and -3 m/s, respectively. The first target serves as a calibration target, while the latter target could be used as a verification target. Subsequently, 1000 frames of the simulated targets were captured using the polarimetric radar system described in Section III-A and processed. For each of the 12 virtual channels, the mean measured phase and amplitude over the 1000 captured frames were computed. The reciprocal of the mean phase and amplitude could subsequently be used as calibration coefficients for the virtual channels. Afterward, the found calibration coefficients were applied to each of the virtual channels and another set of 1000 calibration frames was processed. It was found that for the calibration target, the standard deviation for the worst performing channel was 0.78 dB in amplitude while the standard deviation of the phase was 5.5°. The mean values for the amplitude and phase were found to be below 0.03 dB and 0.38°, respectively. For the verification target, the worst case standard deviations of the amplitude and phase were 0.79 dB and 5.3°, respectively, while the mean values were below 1.26 dB in amplitude and 1.9° in phase. From these results it can be concluded that the calibration procedure was successful, and that systematic errors introduced by differences between channels such as differing feed-line lengths were appropriately compensated.

C. Data Collection

To evaluate the effectiveness of polarimetry for classification of VRUs, multiple classes of VRUs and a car were measured.

Fig. 6. Motorcyclist riding along the measurement area away from the radar.

The measurements were performed in *two different campaigns*. The first was focused on pedestrians and bicyclists, while the second measurement campaign also included measurements of another class of VRU (motorcyclist) as well as a non-VRU (car). Furthermore, the first measurement campaign took place on a grass field in winter time, while the second measurement campaign took place on an asphalt parking lot during spring time.

In the first measurement campaign, five different bicyclists and pedestrians were measured. In the second measurement campaign, three different bicyclists and pedestrians were measured, where 2 of the 3 pedestrians and bicyclists also took part in the first data collection in order to compare measurement results between both campaigns. Besides this, during the second measurement campaign, also a motorcyclist was measured as an additional class of VRU (see Fig. 6), as well as a car representing an example of a non-VRU target.

In both measurement campaigns, each target was measured while moving along four different directions with respect to the radar, namely: toward the radar, away from the radar, diagonally toward the radar, and diagonally away from the radar. The diagonal directions are also denoted by the addition of 45° in the naming convention of the directions. A schematic drawing of the measurement geometry is shown in Fig. 7. All measurements were performed with a single object of interest present within the radar's field of view as this eliminates the need for clustering of detections and tracking, which could potentially form an extra source of error in the final results. Furthermore, each test object was measured three times moving along each direction to obtain statistical information. The measurement procedure can be summarized as follows.

1) Connect the radar system to a power supply and laptop, configure the radar system with the correct waveform parameters mentioned in Table I, and mark the measurement course.
2) Let the test object approach the start marker for one of the four measurement directions, so that the target is at constant speed during the radar measurements.
3) Start the radar measurements when the test object reaches the start marker.
4) Stop the radar measurements when the test object reaches the end marker.
5) Repeat measurements for the measured target moving along the same direction, for three times from step 3.

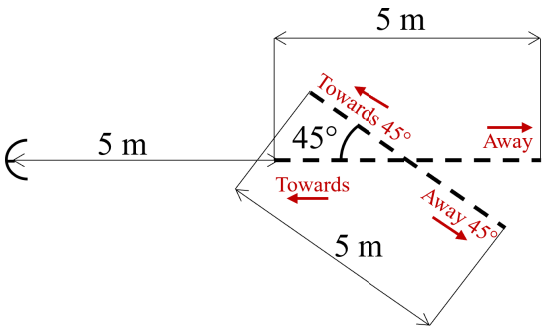

Fig. 7. Schematic representation of the geometry used for polarimetric radar measurements of moving VRUs. The direction identifiers are indicated in red.

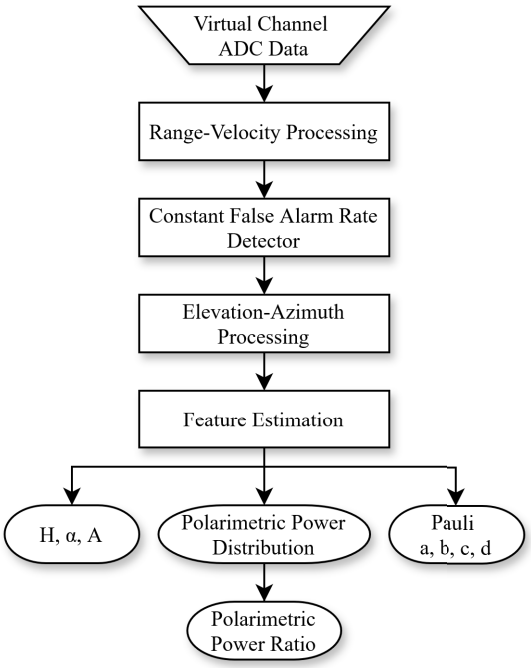

Fig. 8. Block diagram of the postprocessing steps to estimate polarimetric features from the radar measurement data.

6) Repeat measurements for the measured target moving along the remaining three directions from step 3.
7) Repeat measurements for different targets from step 3.

All measurement data were stored locally on a laptop, which could later be transferred to a workstation computer for further processing after the measurements had been completed. Furthermore, the data collected for this work have been made publicly available and can be found in [28].

IV. Measurement Data Postprocessing

To use the data collected during the measurement campaigns for classification purposes, postprocessing must be applied first. A block diagram of this procedure is shown in Fig. 8.

The measurement data is processed similar to the single polarimetric channel processing procedure in Section II-A. The first step in this procedure is to apply range–velocity processing to the raw ADC data. As shown in Section II-A, this can be done by means of FFT over fast time and slow time dimensions for each virtual channel; for both FFTs, here a Kaiser window with a beta value of 6 is used. After transforming the ADC data to the range–velocity domain, a velocity-dependent phase correction is applied to compensate for the phase shift that occurs for moving targets due to TDM, as mentioned in Section II-A.

Unlike for the single channel polarimetric radar data processing procedure in Section II-A, a detector is applied here to the data before performing elevation–azimuth processing. By performing detection on the range–velocity spectra of the individual virtual channels before elevation–azimuth processing, this step needs to be applied only to the range–velocity bins that contain a detection. This greatly reduces requirements on memory and computational resources. The detector used for this purpose first estimates the noise probability density function using samples from an area in the range–velocity plane in which no targets were present during the measurements. The bins in the range–velocity spectrum used for this are those corresponding to velocities in the -7 to -1 m/s and 1 to 7 m/s intervals, and have a range between 15 and 20 m. Subsequently, from this estimate, the detection threshold is determined such that the probability of false alarm is 10^{-15}, resulting in a detector with the constant false alarm rate property. This probability of false alarm was empirically found to provide a good balance between missed detections and false alarms. Furthermore, the bins with velocities between -0.3 and 0.3 m/s are not considered to prevent detections of static clutter. Also, it should be noted that a detection is declared when a value above the aforementioned threshold is found in at least one of the 12 virtual channels, as due to the polarimetric properties of a target, a target may provide a stronger return in some virtual channels, while a weaker return is measured by the virtual channels that correspond to a different polarimetric channel.

After the detection procedure, elevation–azimuth processing is applied on the bins at which a detection was declared. As the apertures of each subarray corresponding to the polarimetric channels are uniform linear arrays, no elevation information can be obtained from single polarimetric channel processing. Therefore, the angular processing is done using steering vectors generated with azimuth values ranging from $-90°$ to $90°$ in $1°$ increments, in combination with an elevation angle of $0°$. This angular processing method also allows to combine the measurement results of all polarimetric channels since they share an equal angular grid, in contrast to performing angular processing using FFTs as the subarrays of the polarimetric channels have different topologies. After angular processing, the angle for which the sum of the squared absolute values of the scattering matrix is maximum is computed. The scattering matrix corresponding to this range–velocity–azimuth bin is then subsequently stored. This procedure effectively selects the dominant target within a range-Doppler cell, thus removing the angular dimension from the processed measurement data. This also mostly compensates for the different angular resolutions of the polarimetric channels as additional targets that may only be visible in polarimetric channels with a high angular resolution are ignored. Dropping the angular dimension also provides lower computational and memory requirements for further processing as an added benefit. The computed dominant scattering matrices of each range-Doppler bin in which a detection took place are subsequently used to compute

several polarimetric features, namely the polarimetric power distribution and corresponding polarimetric power ratios. Furthermore, also the a, b, c, and d values resulting from the Pauli decomposition and the H, α, and A features from the $H\alpha A$-decomposition are considered [29].

The target *polarimetric power distribution* P_{xy} for the xy-polarized channel is defined as the total backscattered power measured by each polarimetric channel, computed over all N range-Doppler bins with detections corresponding to a target within a single frame. This can be mathematically formulated as follows:

$$P_{xy} = \sum_{i=1}^{N} \left| S_{xy}^{i} \right|^2. \tag{16}$$

where N represents the total number of detections corresponding to the observed target within a frame, while S_{xy}^{i} indicates the scattering parameter corresponding to the ith detection.

From the target polarimetric power distribution, the target *polarimetric power ratio* for the xy-polarized channel Q_{xy} can be found. This is defined as the target polarimetric power distribution normalized by the total power scattered back by the target over the N detections. This can be mathematically expressed as shown in the following equation:

$$Q_{xy} = \frac{P_{xy}}{\sum_{i=1}^{N} \left(\left| S_{uu}^{i} \right|^2 + \left| S_{uv}^{i} \right|^2 + \left| S_{vu}^{i} \right|^2 + \left| S_{vv}^{i} \right|^2 \right)}. \tag{17}$$

In this equation, the subscripts u and v are also indicators of the polarization basis, where u corresponds to x and v to y to indicate the sum of the squared magnitudes of all four elements of the scattering matrix. The polarimetric power ratio is independent of the total amount of returned power and thus represents the polarimetric composition of a target. This allows to compare the polarimetric composition of weak targets such as pedestrians, with those of stronger targets like vehicles.

Furthermore, the scattering matrices belonging to the individual detections within a frame can be decomposed to analyze the underlying scattering mechanisms corresponding to a detected target. One of these decompositions is the Pauli decomposition, which decomposes the scattering matrix in four individual scattering mechanisms [29]. As the polarimetric radar system used in this work measures the scattering parameters in a diagonal polarization basis, the first of the *Pauli features*, a, represents the contribution of odd-bounce scattering such as that occurring with scattering from a sphere or plane. The second feature, b, represents scattering from a dihedral with an orientation of 45° with respect to the horizon, while c represents scattering from a dihedral with an orientation of 0° or 90°. Finally, d corresponds to the asymmetric components of the scattering matrix. The a, b, c, and d features can be computed as shown in the following equation:

$$a = \frac{S_{PP} + S_{NN}}{\sqrt{2}}$$
$$b = \frac{S_{PP} - S_{NN}}{\sqrt{2}}$$
$$c = \frac{S_{PN} + S_{NP}}{\sqrt{2}}$$
$$d = j\frac{S_{PN} - S_{NP}}{\sqrt{2}}. \tag{18}$$

Another polarimetric decomposition that can be applied to data from the measurements is the so-called $H\alpha A$-*decomposition*. This decomposition operates on the coherency matrix found from a set of scattering matrices and computes the scattering entropy H, scattering angle α, and scattering anisotropy A. These features are found by performing an eigenvalue decomposition on the coherency matrix from which three eigenvalues λ_1, λ_2, and λ_3 and their corresponding eigenvectors are obtained. Here, subscript 1 corresponds to the largest eigenvalue, while 3 corresponds to the smallest eigenvalue. These eigenvalues are then used to compute three pseudo-probabilities, which are defined as the eigenvalue divided by the sum of the three eigenvalues. More information on the computation of the coherency matrix and pseudo-probabilities can be found in [22] and [29]. The entropy can then subsequently be found as shown in the following equation:

$$H = -\sum_{k=1}^{3} P_k \log_3(P_k). \tag{19}$$

The entropy represents the randomness of the polarimetric response from a target. If all scatterers corresponding to a target are equal, then the coherency matrix will have only one strong eigenvalue leading to an entropy of 0. Conversely, a target comprising of many different polarimetric scatterers will have a high polarimetric entropy.

To compute α, first for each eigenvector a scattering angle α_k is found. This is done by taking the arccosine of the modulus of the first value of the eigenvector. Using the pseudo-probabilities in combination with these three scattering angles, α can be found using the following equation:

$$\alpha = \sum_{k=1}^{3} P_k \alpha_k. \tag{20}$$

When considering a coherency matrix obtained from scatterers corresponding to the same statistically underlying scattering mechanism, the angle α can be used to identify the nature of this scattering mechanism. In the case of performing the $H\alpha A$-decomposition on all detections within a frame, this is no longer necessarily true, as some parts of the measured target may act like a dipole while others act as a flat plate. However, in this scenario α may still contain useful information on the average scattering mechanism of the observed target.

Finally, the polarimetric anisotropy indicates the relative importance of the second and third largest eigenvalue and can be computed via the following equation:

$$A = \frac{\lambda_2 - \lambda_3}{\lambda_2 + \lambda_3}. \tag{21}$$

The polarimetric anisotropy can help to distinguish targets when for example the first eigenvalue is relatively large, thus leading to low entropy, while the second and third eigenvalues are the same or differ significantly from each other.

TABLE II
PERCENTAGE OF TOTAL DETECTIONS BY COMBINING DETECTION RESULTS OF THE POLARIMETRIC CHANNELS INDICATED BY THE ROWS AND COLUMNS

	PP	PN	NP	NN
PP	99.8430	99.8517	99.8641	99.9889
NN	99.9889	99.8961	99.9160	99.8894

V. RESULTS

In this section, the measurement results are analyzed. First, an analysis of the polarimetric data is presented in Section V-A. Subsequently, two classification methods are applied to the measurement data to quantify the information content provided by the polarimetric channels in Sections V-B and V-C. Specifically, in Section V-B, classification is performed on the polarimetric power features, while Section V-C considers classification based on the range–velocity signature using a CNN.

A. Polarimetric Analysis

As described in Section IV, a detection is declared if a detection takes place in any of the virtual channels. However, it is also of interest to consider to what extent including additional polarimetric channels with respect to the co-polarized channels of the radar increases the amount of total detections, in order to investigate the benefits in this regard compared to single-polarized radar systems. Table II shows the amount of detections obtained by combining a co-polar channel and another of the remaining three polarimetric channels as a percentage of total detections obtained by using all four polarimetric channels during the second measurement campaign. It can be seen that including extra polarimetric channels with respect to only the NN- or PP-polarized channels increases the amount of detections slightly. It can be also seen that including the orthogonal co-polarized channel increases the amount of detections the most. This can likely be explained by the observed targets presenting a predominantly strong co-polarized radar cross section.

The first polarimetric feature that is considered is the evolution of the target polarimetric ratios, as defined in (17), as a function of time, as this is an indicator of the stability of the measurement results and the influence of noise. Namely, the target pose/shape with respect to the radar is assumed to remain relatively similar from frame to frame, as the frame repetition time used in these measurements is 10 ms as shown in Table I. Fig. 9 shows the change of the target polarimetric ratios of a bicyclist cycling toward the radar during the last 50 frames measured by the radar. From this figure, it can be seen that the target polarimetric ratios in most cases remain relatively stable from frame to frame, whereas over a longer time span more significant differences are observed. The latter is likely the result of changes in the target pose as the movement progresses during the data recording.

Subsequently, the distribution of the polarimetric ratios in the range–velocity spectrum can also be considered. This can be done by analyzing the polarimetric ratios of the individual detections. They are computed as the ratio of the squared magnitude of the considered scattering parameter divided by

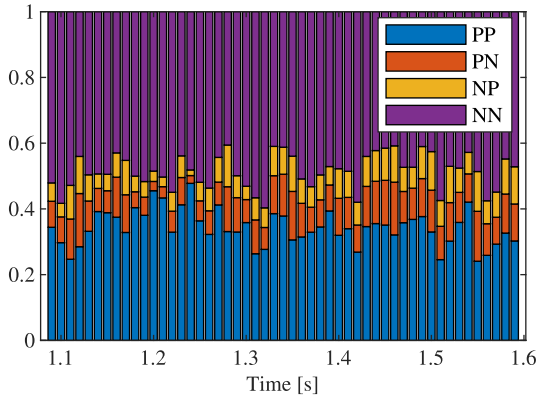

Fig. 9. Target polarimetric ratios as a function of time for a bicyclist cycling toward the radar; the recorded time corresponds to 50 frames.

the squared magnitude of all four scattering parameters for just a single detection, in contrast to the target polarimetric ratio which is computed using all detections corresponding to a target within a frame. Fig. 10 shows the distribution of the polarimetric ratios of each detection in the range–velocity plane. Specifically, in this red, green, and blue (RGB) image, the red channel corresponds to the PP-polarized ratio, the green channel corresponds to the sum of the polarized ratios of the cross-polarized channels, and the blue channel represents the NN-polarized ratio. Thus, the color of each pixel in this figure results from the combination of these three color channels depending on the values of the three polarimetric ratios; for example, a pixel with equal PP- and NN-polarized ratios and negligible cross-polar ratios would map to the color purple as a summation of red and blue colors. The picture on the left-hand side represents a cyclist cycling on a regular bicycle, while the picture on the right-hand side shows a person cycling on a folding bicycle. Even though the bicycles differ from each other, it can be seen that they share a similar polarimetric structure. It can be seen for instance that the rear part of the front wheel of the bicycle provides relatively strong cross-polarized backscattering, while the front part tends to provide a stronger return in the co-polarized channels. Furthermore, it can also be observed that the frame of the bicycle and the cyclist itself also lean toward higher co-polarized backscattering.

A similar comparison between two pedestrians is shown in Fig. 11, adopting the same color mapping of different polarimetric ratios to RGB colors as in Fig. 10. Here it can be seen that the forward swinging limbs exhibit relatively high co-polarized ratios as well as the body itself. The detections corresponding to the backward swinging limbs (i.e., the area with low velocity as well as furthest range) exhibit slightly increased cross-polarized polarimetric ratios with respect to the main body.

Another way of analyzing the involved scattering mechanisms is by considering the Pauli features. The normalized Pauli features for a cyclist riding toward the radar are shown in Fig. 12. From this figure, it can be seen that the a and b features are strongest for the cyclist and bicycle frame, while c is highest for the rear part of the bicycle front wheel. This indicates that the bicycle frame and the cyclist mostly

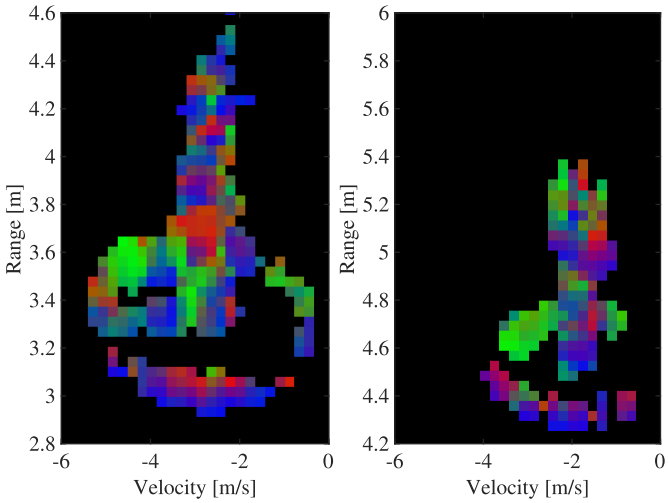

Fig. 10. Distribution of polarimetric ratios of individual detections in the range–velocity plane for cyclists cycling toward the radar on a regular bicycle (left) and a folding bicycle (right). The value of each pixel is given by the combination of the RGB channels representing respectively the PP-polarized ratio, the sum of PN- and NP-polarized ratios, and the NN-polarized ratio.

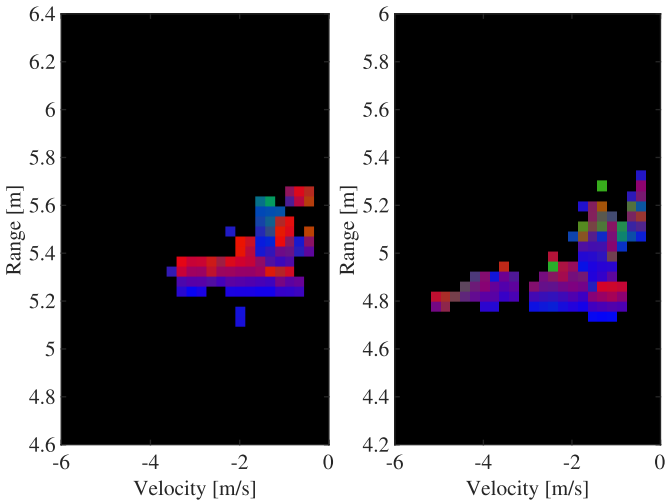

Fig. 11. Distribution of polarimetric ratios of individual detections in the range–velocity plane for two different pedestrians walking toward the radar. The value of each pixel is given by the combination of the RGB channels representing, respectively, the PP-polarized ratio, the sum of PN- and NP-polarized ratios, and the NN-polarized ratio.

provide odd-bounce scattering in combination with scattering mechanisms corresponding to 45°-oriented dihedrals. For the bicycle wheel and spokes, the main scattering mechanism corresponds with scattering from 0°/90°-oriented dihedrals.

Furthermore, it should be noted that the Pauli features are relatively sensitive to noise in the phase measurements of the scattering parameters. The Pauli feature d shows specifically the impact of this characteristic, as for monostatic radar this feature should show no returns. Due to the phase sensitivity of this feature, a phase error of 30° between the measured cross-polar scattering parameters, corresponding to a distance of about 0.3 mm in free space at 77 GHz, already limits the lower bound of the d-feature at about 11 dB below the c-feature. At mm-wave frequencies, this type of measurement error could for example be caused even by thermal expansion effects of the radar board, or small changes between the tightness of the mechanical fasteners after adjustments to account for vibrations when transporting the radar to the measurement campaign location.

Subsequently, the clusters formed by the target polarimeric ratios, computed using all detections within a frame as defined in (17), are considered. Figs. 13 and 14 show the clusters formed by the polarimetric ratios of cyclists and pedestrians as obtained during the first measurement campaign. From these two figures, it can be seen that a cyclist results generally in more cross-polarized backscattering compared to the pedestrian. This can be potentially explained by the vertical and horizontal metal structures of the bicycle frame and wheels, which convert part of the diagonal polarized waves of the radar used in this work to horizontally and vertically polarized waves.

As different classes of targets, besides having different polarimetric ratios, can also return different amounts of power, it is useful to consider this aspect in deriving polarimetric features and then cluster the results. This can be done by looking at clusters formed by the total backscattered power of each channel as defined in (16). Figs. 15 and 16 show this for all target classes moving toward and away from the radar as measured during the second measurement campaign. It can be seen that when also considering the magnitude of the backscattered power, the cluster formed by the car is relatively well separated from the VRU classes. These figures also show that the measured backscattering from the motorcycle behaves similar to that of bicycles, but usually with a stronger return and less variation in cross-polarized scattering.

Comparing Figs. 15 and 16, it can be observed that when also considering the cross-polarized component of the scattering matrix, the separation of the clusters increases and thus that the cross-polarized channels are potentially able to provide useful information for classification purposes. For example, when considering Fig. 15, it is difficult to distinguish the motorcycle and bicycle from each other, but when taking the cross-polarized channel also into consideration it can be seen that the motorcycle becomes more easily separable.

This observation is further reinforced by ranking the polarimetric power features in decibel scale using the Minimum Redundancy Maximum Relevance algorithm [30]. Applying this algorithm to the four polarimetric power features, it is found that the polarimetric power in the PN-polarized channel is the most important, with an importance score of 0.5817, followed by that of the PP-, NP-, and NN-polarized channels, with importance scores of 0.4045, 0.3806, and 0.2434, respectively.

To evaluate the usefulness of measuring both cross-polarized channels, as for an ideal monostatic radar system these features should be equal to each other, the correlation matrices of the polarimetric power are also computed for each class. It is found that for the cyclist, car, and motorcyclist classes, the correlation coefficients of the cross-polarized channels are larger than those of the co-polarized channels, namely 0.9735, 0.9402, and 0.9620 for the cross-polarized channels compared to 0.9731, 0.8858, and 0.9220 for the co-polarized channels, respectively. In contrast, for the pedestrian class, the correlation coefficients of the co-polarized channels are higher than those of the cross-polar channels with values of 0.9432 and

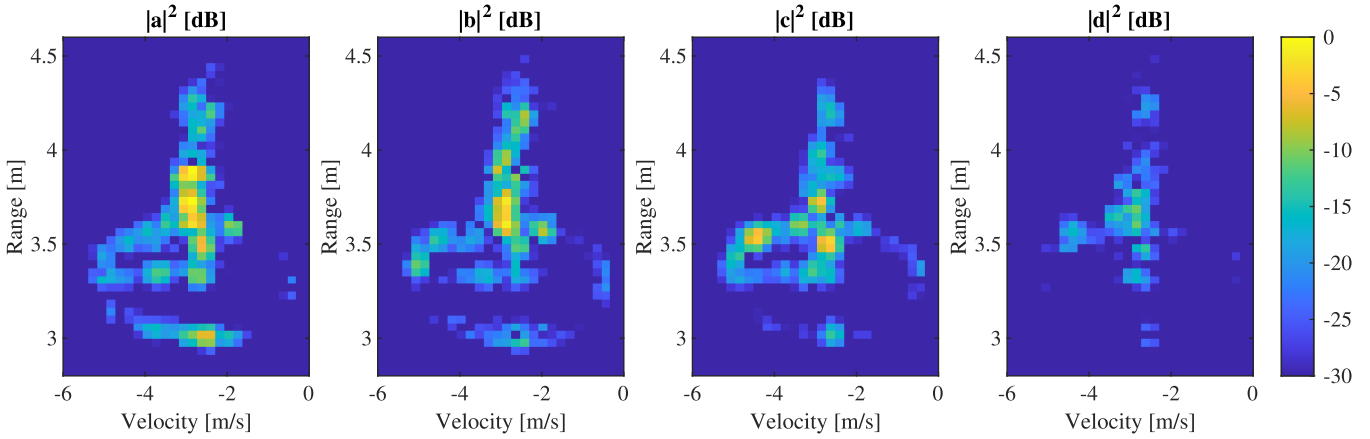

Fig. 12. Normalized Pauli features for a cyclist riding toward the radar in dB scale, normalized with respect to the largest value of the four Pauli features.

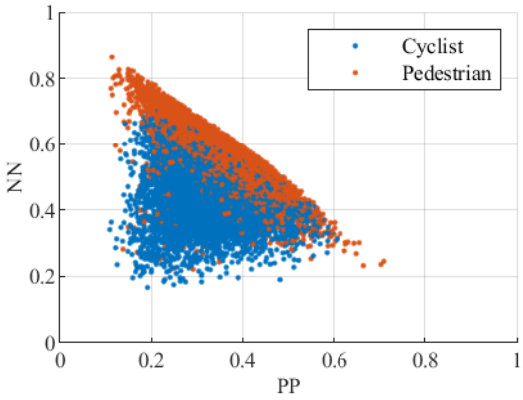

Fig. 13. Clusters formed by the polarimetric ratios for the PP- and NN-polarized channels of cyclists and pedestrians moving toward and away from the radar during the first measurement campaign.

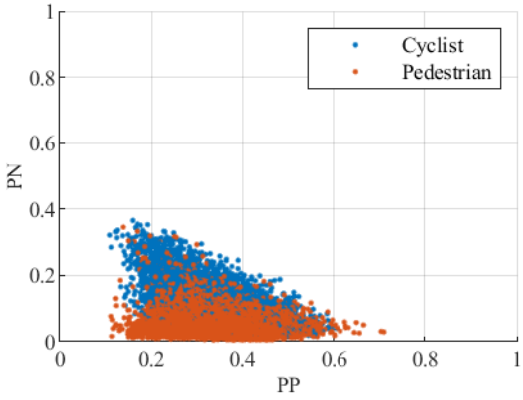

Fig. 14. Clusters formed by the polarimetric ratios for the PP- and PN-polarized channels of cyclists and pedestrians moving toward and away from the radar during the first measurement campaign.

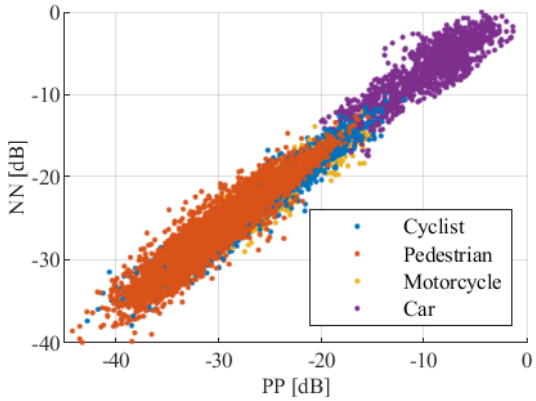

Fig. 15. Clusters formed by the polarimetric power received by the PP and NN channels of a car, a motorcycle, cyclists, and pedestrians moving toward and away from the radar during the second measurement campaign.

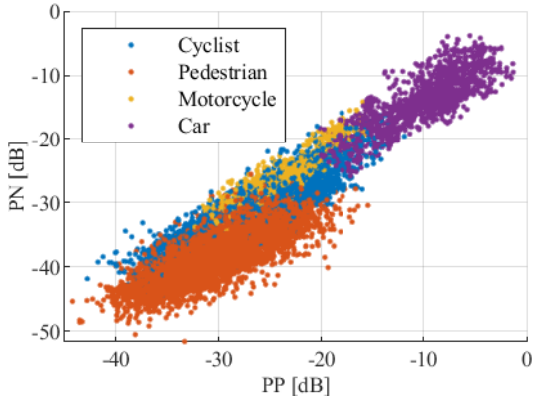

Fig. 16. Clusters formed by the polarimetric power received by the PP and PN channels of a car, a motorcycle, cyclists, and pedestrians moving toward and away from the radar during the second measurement campaign.

0.8832, respectively. This could be explained by the generally weak cross-polarized and strong co-polarized radar cross sections of pedestrians, resulting in the cross-polarized polarimetric power measurements being affected by noise more significantly.

When comparing the clusters formed by the H, α, and A features, shown in Figs. 17 and 18, to the clusters formed by polarimetric power, less separation between clusters is observed. Although each cluster class occupies a specific section in the feature space formed by H, α, and A features, classification based exclusively on these features may be difficult due to the significant overlap between clusters. It can be seen that pedestrians generally have lower entropy than the other classes, as well as a high anisotropy. This indicates that the detections corresponding to the pedestrian within a frame generally have the same polarimetric properties. In contrast, the motorcyclist and cyclist classes have the highest entropy values, indicating that these classes comprise mixtures of different scattering mechanisms. When considering the anisotropy of the bicycle and motorcycle class, it can be

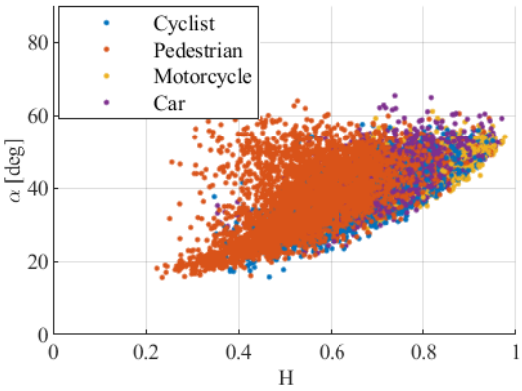

Fig. 17. Clusters formed by the H and α features of a car, a motorcycle, cyclists, and pedestrians moving toward and away from the radar during the second measurement campaign.

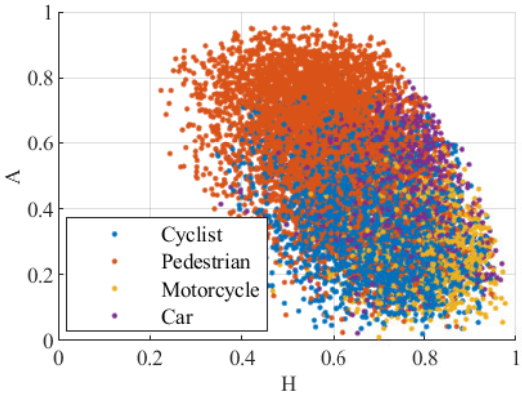

Fig. 18. Clusters formed by the H and A features of a car, a motorcycle, cyclists, and pedestrians moving toward and away from the radar during the second measurement campaign.

seen that the anisotropy values generally range from 0.1 to 0.8, which indicates that scattering matrices corresponding to detections within a frame of these classes show relatively random scattering characteristics.

B. Classification Using Polarimetric Power

To investigate the effectiveness of polarimetry for classification purposes, first a Bayesian classifier based on the polarimetric power feature in dB as shown in Figs. 15 and 16 is employed. This classifier uses Bayes' theorem to compute the probability an observation belongs to a certain class as shown in the following equation:

$$P\left(C_k|\vec{x}\right) = \frac{P(C_k)P\left(\vec{x}|C_k\right)}{P\left(\vec{x}\right)}. \tag{22}$$

In this equation, $\vec{x}$ represents the observed data while C_k indicates the kth class. Furthermore, $P(C_k)$ is the prior belief of the probability to which class the observed data belong to, $P(\vec{x}|C_k)$ the likelihood of the observed data belonging to class C_k, and $P(\vec{x})$ the probability of observing the observed data. This is then used to compute the posterior belief of the probability to which class the observed data belongs, indicated by $P(C_k|\vec{x})$. The posteriors for each class are calculated and the predicted class is then chosen to be the class for which the posterior is the highest. This classifier can be used iteratively over multiple frames, by updating the priors

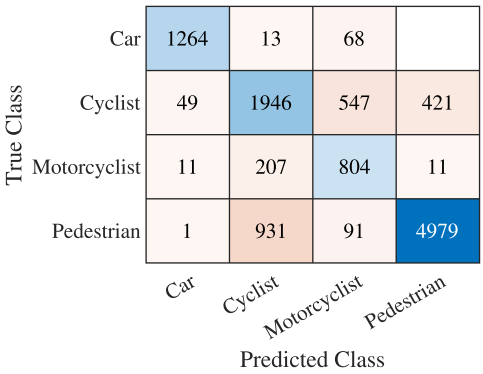

Fig. 19. Confusion matrix for the proposed Bayesian classifier based on the normalized polarimetric power in dB using all polarimetric channels.

with the posteriors found for the previous frame. To compute the likelihood $P(\vec{x}|C_k)$, first the mean vector and covariance values for each cluster formed by the polarimetric power feature in dB are computed. These are then used to assign a multivariate normal distribution to each class. The likelihood can then be determined by evaluating the pdf for the observed data. The probability of observing $\vec{x}$ can then subsequently be determined by multiplying the likelihoods for all classes with their respective priors and summing over them.

In this instance, the priors were selected to be equal for each class. Furthermore, a single frame was used to determine single-frame classification performance. Fig. 19 shows the confusion matrix for this classification approach. As the single-frame classification performance is considered in this confusion matrix, the total number of data points in this matrix is equal to the total amount of frames collected during the second measurement campaign. From this figure, it can be seen that 1264 frames corresponding to cars out of the 1345 total frames containing a car are correctly identified as such, with a corresponding F1-score of 94.7%. Similarly, for pedestrians, the F1-score is 87.3%. For cyclists and motorcyclists, this percentage is significantly lower at 64.2% and 63.2%, respectively. This is likely due to the fact that the cluster formed by the data points corresponding to the cyclists class is spread over a wider area, leading to lower values for the probability density function, which then results in lower probability of classification compared to the motorcyclist class.

To compare classification performance of a polarimetric radar system to a single-polarized counterpart, the same classification procedure was applied to the polarimetric power feature using only the PP-polarized channel. The resulting confusion matrix is shown in Fig. 20. It can be seen that a similar F1-score of 92.6% for cars is achieved compared to the fully polarimetric case, but that F1-scores of the VRU classes have dropped significantly. These values are 73.0%, 34.2%, and 6.7% for the pedestrian, motorcyclist, and cyclist respectively, resulting in a decrease of respectively 14.3, 29.0, and 57.5 percentage points. Thus, especially the cyclist class suffers significantly from not considering the polarimetric features.

From these results, it can be concluded that polarimetric features are able to aid in the classification process of VRUs. It should be noted that the classification performed in

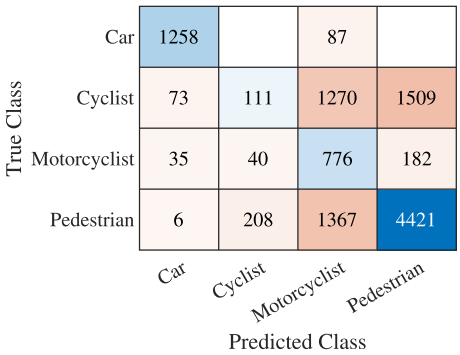

Fig. 20. Confusion matrix for the proposed Bayesian classifier based on the normalized polarimetric power in dB using only the PP-polarized channel (i.e., single polarized approach).

this section is based solely on polarimetric features. Using these features in combination with other (non)polarimetric features and more sophisticated classification procedures could increase classification performance even further.

C. Classification Using Range–Velocity Signatures

Instead of computing a single feature from all detections within a frame as done in Section V-B, classification can also be performed directly on the range–velocity signatures within a frame itself. This approach allows to exploit the (polarimetric) structure of the range–velocity signature, which also can contain useful information for classification.

To investigate the information content provided by the polarimetric structure/patterns formed by the range–velocity signatures, a classifier based on a simple CNN architecture is used. The architecture of the proposed CNN can be modeled by five layers, namely in order: an input layer, a convolutional layer with 32 3×3 filters, a fully connected layer with four outputs, a softmax layer to act as a nonlinear activation layer, and a final classification output layer. The input to the network is a 3-D tensor, where the first and second dimensions correspond to range and velocity, while the third represents each polarimetric channel. Also, an equivalent CNN for single-polarized radar data was setup with the same architecture, which uses only one of the four polarimetric channel.

The input data to the networks was normalized in two ways, in decibel scale and polarimetric ratios. For the decibel normalization, the frames are first transformed to decibel, and subsequently scaled so that the strongest detection in the strongest polarimetric channel within the frame corresponds to a value of 1, while the weakest return in the weakest polarimetric channel of that same frame corresponds to 0. For the single-polarimetric reference, the PP-polarized layer of the normalized data was used.

The second normalization method uses the polarimetric ratios of each detection. As the polarimetric ratios for each detection sum to 1, no further normalization is required. For the single-polarized variant of the network, all detections were given a value of 1. This means that in this case both single-polarized and fully polarized classification networks have the same shape information, obtained using all polarimetric channels, whereas the fully polarized network also has access to the polarimetric ratios of the detections.

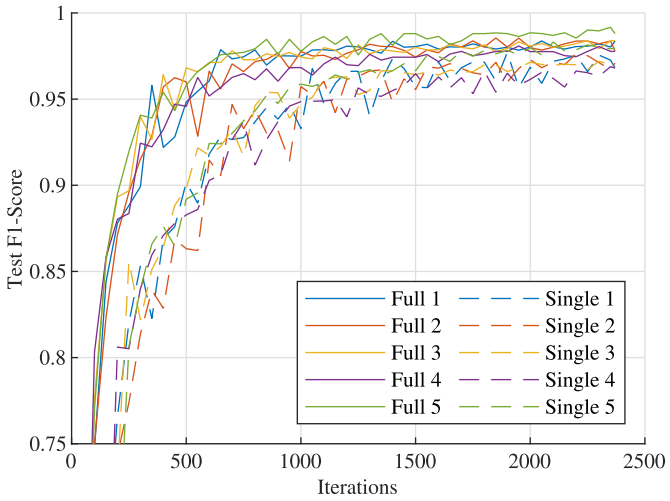

Fig. 21. F1-score of the test set for decibel-scale input normalization after the indicated number of completed training iterations for both fully and single-polarized classifiers.

For both normalization methods, the data was split into five different test and training sets on which both the fully and single-polarized classifiers were trained, resulting in ten trained networks. Each of the splits was chosen such that for each class, 90% of the frames corresponding to that class were used for training, while the remaining 10% was used for testing, resulting in each test set containing 135, 296, 103, and 600 frames corresponding to the car, cyclist, motorcyclist, and pedestrian class, respectively. This allows for evaluating the spread in classification performance due to the difference in training and test datasets, where one training dataset may result in a slightly better test accuracy than another. Furthermore, training was performed with the stochastic gradient descent optimizer, a learning rate of 0.001, and a mini-batch size of 128. Each network was trained for 30 epochs at which no large improvements in test accuracy were observed anymore, and hence the training process was stopped.

Fig. 21 shows the F1-scores for the test sets as a function of the number of training iterations performed for decibel-scale normalization. It can be seen that both single- and fully polarized classifiers achieve a similar mean F1-score, of respectively 97.2% and 98.2%. Thus, the fully polarized classifier achieves a slightly better result. It can also be noticed that the fully polarized network is able to achieve higher F1-score earlier than the single-polarized one, thus indicating that useful information is present in the polarimetric channels for classification purposes.

Fig. 22 shows that for the polarimetric ratios, similar performance between the fully and single-polarized classifiers is achieved of respectively 98.6% and 99.7%. In contrast to decibel-normalized data, the single-polarized network performs better for the ratio-normalized data compared to the fully polarimetric network. Also, the single-polarized network achieves higher test set F1-score with fewer iterations than the fully polarimetric classifier.

From this, it can be concluded that the shape of the range–velocity signature is most likely the most significant factor in achieving good classification performance, and that in this case the ratio information "distracted" the fully

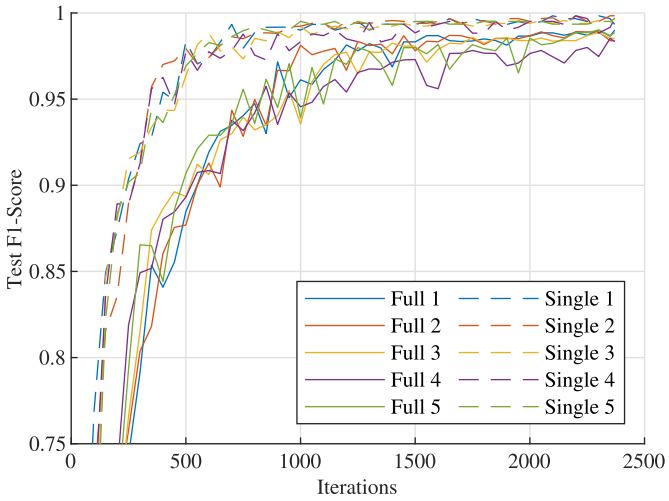

Fig. 22. F1-score of the test set for polarimetric ratio input normalization after the indicated number of completed training iterations for both fully and single-polarized classifiers.

polarimetric network. This is further supported by the results obtained from the decibel-scaled data, since other polarimetric channels may contain strong returns that are weak in the channel used by the single-polarized classifier, thus enhancing the contrast of the range–velocity signature. Thus, this shows that polarimetric radar does result in better classification performance using a simple CNN-based classifier as the diversity in polarimetric channels results in more detections, and therefore a higher contrast range–velocity signature, which may be missed when using only a single-polarized radar system. The lagging classification performance of the fully polarimetric network for the ratio-normalized data shows that in order to properly exploit the polarimetric information, more complex polarimetric features and/or networks are likely needed.

Figs. 23 and 24 show the confusion matrices for the decibel-normalized input networks generated by summing the classification results of all five classifiers of their corresponding test sets, thus resulting in a total amount of 675, 1480, 515, and 3000 data points for the car, cyclist, motorcyclist, and pedestrian class, respectively. Fig. 23 shows the results for the fully polarized classifier, while Fig. 24 shows the results for the single-polarized classifier. It can be seen that for both classifiers most misclassifications occur between cyclists and motorcyclists. This is expected as the shapes of the range–velocity signatures of cyclists and motorcyclists are similar to each other. Similar behavior is observed for the ratio-based fully and single-polarized classifiers shown in Figs. 25 and 26, respectively.

To summarize, Table III shows the F1-scores achieved by the networks. It can be seen that the F1-scores of all classes are relatively similar, with the F1-scores for the motorcyclist being the lowest. This can be explained by this class having the least available frames for training and testing out of all classes, while having a similar signature as the cyclist. Furthermore, it can be seen that the F1-scores are highest for the single-polarized ratio-normalized input classifier, thus further reaffirming the explanation provided in the previous paragraphs.

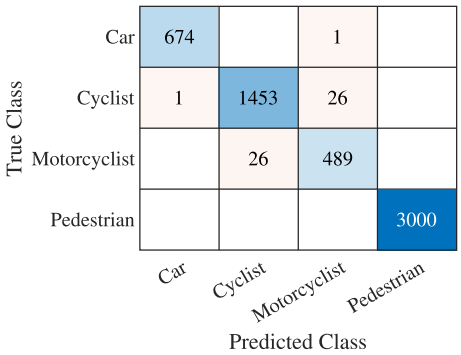

Fig. 23. Confusion matrix for the proposed CNN-based classifier using the fully polarimetric decibel-normalized input data format.

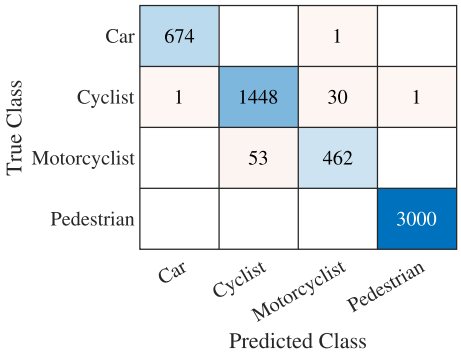

Fig. 24. Confusion matrix for the proposed CNN-based classifier using the decibel-normalized input data format with only a single polarimetric channel.

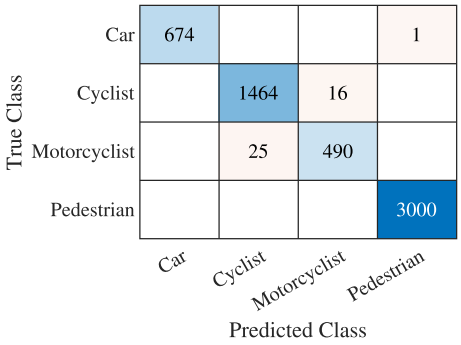

Fig. 25. Confusion matrix for the proposed CNN-based classifier using the fully polarimetric ratio-normalized input data format.

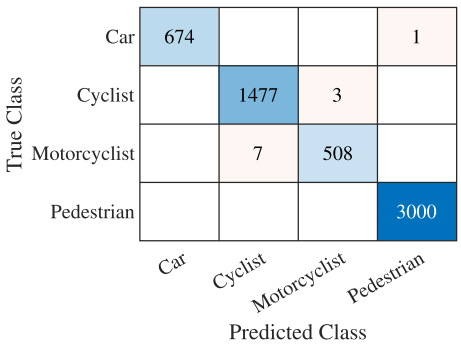

Fig. 26. Confusion matrix for the proposed CNN-based classifier using the ratio-normalized input data format with only a single polarimetric channel.

Finally, the importance of the cross-polar polarimetric channels for classification is considered. To this end, instead of training the single-polarized decibel-normalized network with only the PP-polarized polarimetric channel, this network was modified by adding an extra input layer for the NN-polarized channel. This resulted in F1-scores of 99.9%, 97.7%, 93.7%,

TABLE III
F1-SCORES ACHIEVED BY FULLY AND SINGLE-POLARIZED CLASSIFIERS USING DECIBEL- AND RATIO-NORMALIZED INPUT DATA

	dB Scaled		Ratio Scaled	
	Full	**Single**	**Full**	**Single**
Car	0.999	0.999	0.999	0.999
Cyclist	0.982	0.971	0.986	0.997
Motorcyclist	0.949	0.917	0.960	0.990
Pedestrian	1.000	1.000	1.000	1.000

and 100% for the car, cyclist, motorcyclist, and pedestrian class, respectively. From this, it can be concluded that there is indeed to a certain extent information present in the depolarization caused by a target, as the F1-scores are slightly lower than those obtained with its fully polarized counterpart and slightly higher than its single-polarized version.

VI. CONCLUSION

In this article, a novel method for classifying VRUs using polarimetric MIMO radar is proposed. To this end, a signal processing pipeline was proposed using virtual channels that correspond to the same polarimetric channel. The method comprises of range–velocity processing using FFTs and angular processing using digital beam forming, including a velocity-dependent phase correction to account for phase changes of moving targets that occur due to TDM used in automotive radar. To reduce loss of angular resolution that occurs when using a polarimetric radar, a combined polarimetric channel processing method is also introduced. This method allows to successfully enhance the angular resolution compared to single-polarimetric channel processing. It is also shown that when a radar system provides good polarimetric diversity, it is possible to outperform single-polarized radar systems for targets that have low returns in the polarimetric channel of the single-polarized system while providing a strong return in others.

This processing pipeline has been applied to the data coming from a polarimetric MIMO automotive radar, which was developed in collaboration with Huber+Suhner AG based on the AWR2243BOOST module by Texas Instruments. The developed radar uses a diagonal polarization basis and is calibrated using a new active calibration method, allowing to calibrate all virtual channels at once, independent of polarization. Using this radar system, multiple different moving target classes were measured, namely, pedestrian, cyclist, motorcyclist, and car. From their measurements, multiple different polarimetric features were extracted and analyzed. It is found that the polarization ratios of pedestrians are relatively high, while other classes comparatively provide more cross-polar backscattering.

Using exclusively the proposed feature of target polarimetric power, it is shown that a Bayesian classifier was able to achieve an F1-score of 94.7%, 87.3%, 63.2%, and 64.2% for cars, pedestrians, motorcyclists, and cyclists, respectively. It is found that by not including the polarimetric properties, the F1-scores of the VRU classes dropped significantly, especially in the case of cyclists, which decreased from 64.2% to 6.7%. The F1-scores for pedestrians and motorcyclists dropped from 87.3% to 73.0% and from 63.2% to 34.2%, respectively. From this, it can be concluded that polarimetric information provides beneficial information for VRU classification and that it can be used to boost classification performance compared to single-polarized radar systems. Additionally, a CNN-based classifier was also used to classify the measured targets, exploiting the "spatial" distribution of polarimetric features in their range–velocity spectra. Here, it was found that polarimetric radar is beneficial as it is able to provide clearer range–velocity signatures due to polarization diversity. To fully exploit polarimetric information available in range–velocity signatures, more complex polarimetric features and/or a more complex network architecture are likely required.

Even though the classifiers have been applied to measurement data with one object per frame, the proposed classification procedures can be extended to scenarios with multiple targets by implementing a clustering step after detection to separate multiple targets. The proposed classifiers can then subsequently be applied to the individual clusters. This could in turn be used to enhance subsequent tracking steps, as polarimetric features provide an extra source of distinguishing information which could for example help with assigning the correct tracks to two clusters that merge and then separate again, or help with assigning a suitable target motion model to a selected cluster.

Furthermore, to fully extract maximum performance from polarimetric MIMO radar systems, although negligible in the measurement results presented in this work, compensating the impact of nonlinear effects that can occur in FMCW waveforms due to practical limitations of chirp generation circuitry may also be considered in future research.

ACKNOWLEDGMENT

The authors would like to thank Alejandro Garcia-Tejero from Huber+Suhner AG for his contributions to the development of the polarimetric radar system used in this work.

REFERENCES

[1] M. V. I. en Waterstaat. *Actuele Verkeersongevallencijfers*. Accessed: Mar. 12, 2024. [Online]. Available: http://www.rijkswaterstaat.nl/wegen/wegbeheer/onderzoek/verkeersveiligheid-en-ongevallencijfers/actuele-verkeersongevallencijfers

[2] M. Dimitrievski, I. Shopovska, D. V. Hamme, P. Veelaert, and W. Philips, "Weakly supervised deep learning method for vulnerable road user detection in FMCW radar," in *Proc. IEEE 23rd Int. Conf. Intell. Transp. Syst. (ITSC)*, Sep. 2020, pp. 1–8.

[3] D. Wachtel, J. Edler, S. Schröder, S. Queiroz, and W. Huber, "Convolutional neural network classification of vulnerable road users based on micro-Doppler signatures using an automotive radar," in *Proc. IEEE 25th Int. Conf. Intell. Transp. Syst. (ITSC)*, Oct. 2022, pp. 866–872.

[4] R. Pérez, F. Schubert, R. Rasshofer, and E. Biebl, "Single-frame vulnerable road users classification with a 77 GHz FMCW radar sensor and a convolutional neural network," in *Proc. 19th Int. Radar Symp. (IRS)*, Jun. 2018, pp. 1–10.

[5] P. Rippl, J. Iberle, and T. Walter, "Classification of vulnerable road users based on spectrogram autocorrelation features," in *Proc. 18th Eur. Radar Conf. (EuRAD)*, Apr. 2022, pp. 293–296.

[6] R. Prophet, M. Hoffmann, A. Ossowska, W. Malik, C. Sturm, and M. Vossiek, "Image-based pedestrian classification for 79 GHz automotive radar," in *Proc. 15th Eur. Radar Conf. (EuRAD)*, Sep. 2018, pp. 75–78.

[7] G. F. Hamberger, S. Späth, U. Siart, and T. F. Eibert, "A mixed circular/linear dual-polarized phased array concept for automotive radar—Planar antenna designs and system evaluation at 78 GHz," *IEEE Trans. Antennas Propag.*, vol. 67, no. 3, pp. 1562–1572, Mar. 2019.

[8] A. Tinti, S. T. Alfageme, S. D. Biarge, and N. Pohl, "Full polarimetric antenna system for automotive radar," in *Proc. IEEE Topical Conf. Wireless Sensors Sensor Netw.*, Jan. 2023, pp. 39–42.

[9] S. Trummer, G. F. Hamberger, U. Siart, and T. F. Eibert, "A polarimetric 76–79 GHz radar-frontend for target classification in automotive use," in *Proc. Eur. Radar Conf. (EuRAD)*, Oct. 2016, pp. 346–349.

[10] Z. Zang, Q. Ren, A. Uz Zaman, and J. Yang, "77 GHz fully polarimetric antenna system with compact circularly polarized slots in gap waveguide for automotive radar," *IEEE Trans. Antennas Propag.*, vol. 72, no. 7, pp. 5578–5588, Jul. 2024.

[11] A. Tinti, S. Tejero Alfageme, S. D. Biarge, J. Balcells-Ventura, and N. Pohl, "Fully polarimetric automotive radar: Proof of concept," *IEEE Trans. Radar Syst.*, vol. 2, pp. 645–660, 2024.

[12] A. Y. Nashashibi, T. J. Douglas, M. Kashanianfard, S. W. Decker, and K. Sarabandi, "High-resolution polarimetric radar for autonomous vehicle research at W-band frequencies," *IEEE Trans. Radar Syst.*, vol. 2, pp. 632–644, 2024.

[13] J. F. Tilly, O. Schumann, F. Weishaupt, J. Dickmann, and G. Waniliek, "Polarimetric information representation for radar based road user detection with deep learning," in *Proc. IEEE 24th Int. Conf. Inf. Fusion (FUSION)*, Nov. 2021, pp. 1–6.

[14] J. F. Tilly, F. Weishaupt, O. Schumann, J. Dickmann, and G. Wanielik, "Road user classification with polarimetric radars," in *Proc. 17th Eur. Radar Conf. (EuRAD)*, Jan. 2021, pp. 112–115.

[15] O. Schumann, J. Lombacher, M. Hahn, C. Wöhler, and J. Dickmann, "Scene understanding with automotive radar," *IEEE Trans. Intell. Vehicles*, vol. 5, no. 2, pp. 188–203, Jun. 2020.

[16] J. F. Tilly, F. Weishaupt, O. Schumann, J. Dickmann, and G. Wanielik, "Road user detection on polarimetric pre-CFAR radar data level," *IEEE Robot. Autom. Lett.*, vol. 8, no. 6, pp. 3558–3565, Jun. 2023.

[17] F. Weishaupt, J. F. Tilly, N. Appenrodt, P. Fischer, J. Dickmann, and D. Heberling, "Landmark-based vehicle self-localization using automotive polarimetric radars," *IEEE Trans. Intell. Transp. Syst.*, vol. 25, no. 10, pp. 14266–14283, Oct. 2024.

[18] T. Visentin, J. Hasch, and T. Zwick, "Polarimetric RCS measurements of selected two-wheeled vehicles for automotive radar," in *Proc. Eur. Radar Conf. (EURAD)*, Oct. 2017, pp. 53–56.

[19] K. Geary, J. S. Colburn, A. Bekaryan, S. Zeng, B. Litkouhi, and M. Murad, "Automotive radar target characterization from 22 to 29 GHz and 76 to 81 GHz," in *Proc. IEEE Radar Conf. (RadarCon)*, Ottawa, ON, Canada, Apr. 2013, pp. 1–6.

[20] T. Visentin, A. Sagainov, J. Hasch, and T. Zwick, "Classification of objects in polarimetric radar images using CNNs at 77 GHz," in *Proc. IEEE Asia–Pacific Microw. Conf. (APMC)*, Nov. 2017, pp. 356–359.

[21] J. Bechter, F. Roos, and C. Waldschmidt, "Compensation of motion-induced phase errors in TDM MIMO radars," *IEEE Microw. Wireless Compon. Lett.*, vol. 27, no. 12, pp. 1164–1166, Dec. 2017.

[22] W. Bouwmeester, F. Fioranelli, and A. G. Yarovoy, "Road surface conditions identification via HαA decomposition and its application to mm-wave automotive radar," *IEEE Trans. Radar Syst.*, vol. 1, pp. 132–145, 2023.

[23] U. Huegel, A. Garcia-Tejero, R. Glogowski, E. Willmann, M. Pieper, and F. Merli, "3D waveguide metallized plastic antennas aim to revolutionize automotive radar," *Microw. J.*, vol. 65, no. 9, p. 32, Sep. 2022.

[24] A. Garcia-Tejero, F. R. Varela, R. Torres-Sánchez, M. Burgos-Garcia, and F. Merli, "Wideband untilted narrow wall slotted partially staggered waveguide array based on metallized molded plastic at E-band," *IEEE Antennas Wireless Propag. Lett.*, vol. 23, pp. 915–919, 2024.

[25] A. Garcia-Tejero, M. Burgos-García, and F. Merli, "Broadband metalized plastic waveguide antenna with robust isolation interface at 77 GHz," *IEEE Antennas Wireless Propag. Lett.*, vol. 23, no. 10, pp. 2875–2879, Oct. 2024.

[26] C. Zhao, A. Garcia-Tejero, W. Bouwmeester, Y. Aslan, O. Krasnov, and A. Yarovoy, "Calibration of polarimetric automotive radar with asymmetric MIMO topology and off-broadside beamforming," in *Proc. 21st Eur. Radar Conf. (EuRAD)*, Sep. 2024, pp. 87–90.

[27] F. Weishaupt, J. F. Tilly, N. Appenrodt, J. Dickmann, and D. Heberling, "Calibration and signal processing of polarimetric radar data in automotive applications," in *Proc. Microw. Medit. Symp.*, May 2022, pp. 1–6.

[28] W. Bouwmeester, F. Fioranelli, and A. Yarovoy, "Dataset of moving vulnerable road users and vehicle using a fully polarimetric mm-wave MIMO radar," TU Delft, Delft, The Netherlands, 2024, doi: 10.4121/7e080aea-2a1b-4262-834c-9a8d926f2474.

[29] J.-S. Lee and E. Pottier, *Polarimetric Radar Imaging: From Basics to Applications*. Boca Raton, FL, USA: CRC Press, Jan. 2017.

[30] C. Ding and H. Peng, "Minimum redundancy feature selection from microarray gene expression data," *J. Bioinf. Comput. Biol.*, vol. 3, no. 2, pp. 185–205, Apr. 2005.

Wietse Bouwmeester (Member, IEEE) received the B.Sc. degree in electrical engineering from Delft University of Technology (TU Delft), Delft, The Netherlands, in 2016, the M.Sc. degree in electrical engineering from TU Delft, in 2020, with a focus on telecommunications and sensing systems, and the Ph.D. degree from TU Delft, in 2024. He graduated cum laude on the design of a conformal phased array antenna commissioned by ASTRON, the Dutch institute for radio astronomy.

In May 2020, he joined the Microwave Sensing, Signals and Systems Group, TU Delft, where he worked on polarimetric approaches to classify road surfaces and other targets with mm-wave radar for automotive applications. In September 2024, he received the Ph.D. degree for his contributions to this research topic.

Francesco Fioranelli (Senior Member, IEEE) received the Laurea (B.Eng., cum laude) and Laurea Specialistica (M.Eng., cum laude) degrees in telecommunication engineering from the Università Politecnica delle Marche, Ancona, Italy, in 2007 and 2010, respectively, and the Ph.D. degree from Durham University, Durham, U.K., in 2014.

He was a Research Associate at University College London, London, U.K., from 2014 to 2016, and an Assistant Professor at the University of Glasgow, Glasgow, U.K., from 2016 to 2019. He is currently an Associate Professor at TU Delft, Delft, The Netherlands. He has authored over 190 peer-reviewed publications, edited the books titled *Micro-Doppler Radar and Its Applications* and *Radar Countermeasures for Unmanned Aerial Vehicles*published by IET-Scitech in 2020. His research interests include the development of radar systems and automatic classification for human signatures analysis in healthcare and security, drones and UAVs detection and classification, automotive radar, wind farm, and sea clutter.

Dr. Fioranelli received four best paper awards and the IEEE AESS Fred Nathanson Memorial Radar Award in 2024.

Alexander G. Yarovoy (Fellow, IEEE) received the Diploma degree (Hons.) in radiophysics and electronics and the Candidate Phys. & Math. Sci. and Doctor Phys. & Math. Sci. degrees in radiophysics from Kharkov State University, Kharkiv, Ukraine, in 1984, 1987, and 1994, respectively.

In 1987, he joined the Department of Radiophysics, Kharkov State University, as a Researcher and became a Full Professor there in 1997. From September 1994 to 1996, he was with the Technical University of Ilmenau, Ilmenau, Germany, as a Visiting Researcher. Since 1999, he has been with Delft University of Technology, Delft, The Netherlands. Since 2009, he leads the Microwave Sensing, Systems and Signals Group as the Chair. He has authored and co-authored more than 600 scientific or technical papers, 11 patents, and 14 book chapters. His main research interests are in high-resolution radar, microwave imaging, and applied electromagnetics (in particular, UWB antennas).

Dr. Yarovoy has been a member of numerous conference steering and technical program committees. He was a recipient of the European Microwave Week Radar Award for the paper that best advances the state-of-the-art in radar technology in 2001 (together with L. P. Ligthart and P. van Genderen) and in 2012 (together with T. Savelyev). In 2023, together with Dr. I. Ullmann, N. Kruse, R. Gündel, and Dr. F. Fioranelli he got the Best Paper Award at IEEE Sensor Conference. In 2010, together with D. Caratelli Prof. Yarovoy got the Best Paper Award of the Applied Computational Electromagnetic Society (ACES). In the period 2008–2017, he served as the Director of the European Microwave Association (EuMA). He has been serving on various editorial boards such as that of IEEE TRANSACTION ON RADAR SYSTEMS. From 2011 to 2018, he served as an Associate Editor for *International Journal of Microwave and Wireless Technologies*. He served as the General TPC Chair for the 2020 European Microwave Week (EuMW'20), as the Chair and the TPC Chair for the 5th European Radar Conference (EuRAD'08), as well as the Secretary for the 1st European Radar Conference (EuRAD'04). He also served as the Co-Chair and the TPC Chair for the Xth International Conference on GPR (GPR2004).